npj Computational Materials

https://doi.org/10.1038/s41524-026-02058-1

Article in Press

Structure divide-and-conquer: dual graph representation for accurate ionic transport barrier prediction of inorganic compounds

Received: 19 September 2025

Accepted: 15 March 2026

Cite this article as: Yang, Z., Wu, L., He, B. *et al.* Structure divide-and-conquer: dual graph representation for accurate ionic transport barrier prediction of inorganic compounds. *npj Comput Mater* (2026). https://doi.org/10.1038/s41524-026-02058-1

Zhengwei Yang, Linhan Wu, Bing He, Maxim Avdeev, Siqi Shi & Yue Liu

Structure Divide-and-Conquer: Dual Graph Representation for Accurate Ionic Transport Barrier Prediction of Inorganic Compounds

Zhengwei Yang[1], Linhan Wu[1], Bing He[1], Maxim Avdeev[3], Siqi Shi[2, 4, *], Yue Liu[1, *]

[1]*School of Computer Engineering and Science & State Key Laboratory of Materials for Advanced Nuclear Energy, Shanghai University, Shanghai 200444, China*

[2]*State Key Laboratory of Materials for Advanced Nuclear Energy & School of Materials Science and Engineering, Shanghai University, Shanghai 200444, China*

[3]*School of Chemistry, The University of Sydney, Sydney 2006, Australia*

[4]*Materials Genome Institute, Shanghai University, Shanghai 200444, China*

[*]Corresponding author: (E-mail: sqshi@shu.edu.cn; yueliu@shu.edu.cn)

Abstract

Despite the effectiveness of most graph-based representation methods in capturing the crystal geometry characteristics, they fall short in intuitively describing phenomena such as ionic transport behavior which are often determined by the atom-unoccupied regions in the mobile sublattice (namely interstitial network). Here, we develop a Structure Divide-and-Conquer Graph Representation method based on graph neural network ($SDCGNN_{dk}$), for unveiling structure-activity relationships of transport barriers by incorporating Domain Knowledge (e.g., site energy information, thresholds for ion accessibility, etc.), where crystal geometry and interstitial network topology are combined to construct a dual-structure crystal graph. For driving the proposed model, we construct a graph-based dataset for the prediction of activation energy (E_a), i.e., the energy barrier hindering ionic transport, covering over 18,000 ionic compounds from the Inorganic Crystal Structure Database (ICSD), including Li^+, Na^+, K^+, Ag^+, $Cu^{(2, 3)+}$, Mg^{2+}, Zn^{2+}, Ca^{2+}, Al^{3+}, F^-, and O^{2-}. $SDCGNN_{dk}$ achieves high prediction performance of E_a with R^2 of 91.30 %, outperforming conventional GNNs by more than 20% on average and offering insights into structure-activity relationships by quantifying the contributions of crystal geometry and interstitial network characteristics to transport barriers. This work provides an accurate graph representation and GNN framework, demonstrating potential for extension to predicting other properties relevant to interstitial network of inorganic compounds.

Keywords: Materials Science; Graph Neural Networks; Structure Divide-and-Conquer; Domain Knowledge

INTRODUCTION

Data-driven machine learning (ML) exhibits substantial potential in the discovery of new fast ionic conductors due to its ability to quickly find structure-activity relationships for materials [1-3]. By training ML models on structured materials data, researchers can develop predictive models that can guide the design and synthesis of new functional materials with desired properties [4-6]. One of the limiting factors of these ML models is the requirement for cumbersome feature engineering to construct structured descriptors, which may introduce potential biases and limit the model's performance and generalization ability.

Recently, graph representation of material structure, based on graph neural networks (GNNs), has been shown to be a powerful tool in accurately predicting materials property [7,8]. For example, Ahmad et al. [9] trained a graph convolutional network to predict shear modulus and bulk modulus of inorganic solid electrolytes. Louis et al. [10] used attention-based graph neural networks to predict voltage of battery electrode materials. While GNNs provide a way to establish material structure-activity relationships at the atomic level, there are still two critical challenges: (1) the graph representation of material structure typically relies on external crystal geometry, neglecting the significant influence of other features of the interstitial network on describing ionic transport pathways; (2) most GNNs are purely data-driven and lack the integration with domain knowledge. These constraints hinder GNN's ability to fully extract structure-activity relationships of transport barrier in inorganic compounds. It is a pressing need to develop a new perspective on materials graph representation and effective GNN modelling approaches to achieve the accurate prediction of transport activation energy barriers.

Ionic transport is affected not only by the crystal geometry (CG) formed by atoms[11], but also by the connectivity of the interstitial network (IN). These two distinct aspects can influence ion transport behavior in complementary ways. By integrating both perspectives, along with the powerful feature extraction capabilities of GNNs, a more comprehensive understanding of the ion transport structure-activity relationships can be achieved. Furthermore, researchers have accumulated substantial domain knowledge and effectively leveraging them is critical for enhancing the interpretability and generalization of ML models. As discussed in our previous review [12,13], the different forms of domain knowledge can be represented various types and embedded into the entire process of ML modelling, e.g., those found in chemically-motivated

descriptors [14] or physics-informed neural network architectures [15], that can significantly improve the interpretability and generalizability of data-driven models. This work focuses on improving effectiveness of GNN method by incorporating domain knowledge into the GNN modelling process.

To this end, we propose a Structure Divide-and-Conquer Graph Neural Network framework by incorporating Domain Knowledge ($SDCGNN_{dk}$), aiming to unveil structure-activity relationships of transport activation energy barriers. Concisely, a novel crystal graph representation method based on divide-and-conquer approach is introduced. Unlike the input information based on a single CG perspective in previous work [16-21], we combine it with the information on the IN to construct crystal graph representation. In addition, we incorporate structural representation of materials domain knowledge (e.g., thresholds for ion accessibility) into the message passing mechanisms of GNNs so that new GNN models with high accuracy can be constructed and a collaborative integration of data and domain knowledge can be realized in third-generation artificial intelligence. The results demonstrate that $SDCGNN_{dk}$ can fully extract ion transport features and achieve high prediction performance of transport activation energy barrier. Finally, to fully integrate the structure information from different perspectives of material structure, we explore several feature fusion strategies from feature level to decision level to hybrid level to model level. Our work lays a foundation for comprehensively unveiling structure-activity relationships of transport barrier and accelerates the discovery and design of new ionic conductors.

RESULTS

$SDCGNN_{dk}$ architecture

As shown in **Fig.1**, $SDCGNN_{dk}$ leverages the Voronoi algorithm to decompose complex crystal space into two distinct substructures: crystal geometry (CG) and interstitial network (IN), thereby implementing the "divide" step of the "divide-and-conquer" strategy to deconstruct intricate ionic transport aspects. Then, recognizing the mechanistic divergence in how these substructures influence ionic transport property, a dual graph representation integrating CG and IN is constructed to accurately characterize ion migration behavior. Subsequently, to effectively execute the "conquer" step for the decomposed subproblems, two domain-knowledge-integrated GNNs are constructed to jointly extract topological connectivity and ion transport features. To

further boost representational capabilities of the model, a hybrid-level feature fusion strategy based on structural importance is designed, where an adaptive weighting mechanism is introduced to dynamically adjust the contributions of different substructures in the high-dimensional representation space, achieving deep coupling of heterogeneous information across structural domains. As a result, a highly discriminative structure representation vector is obtained to accurately unveil the structure-activity relationships of ionic transport barriers.

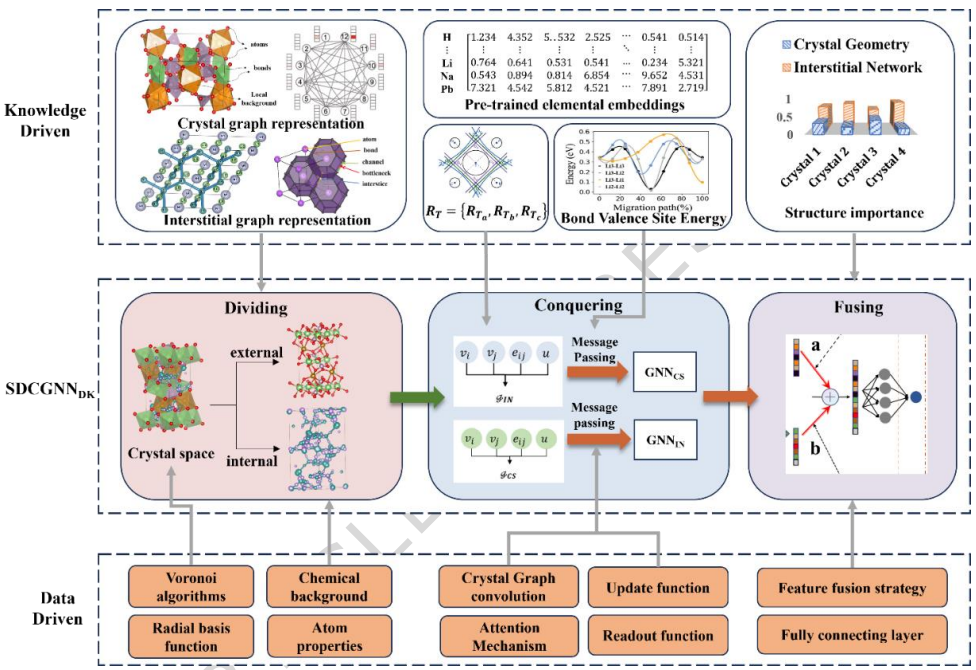

Fig.1. The overall framework of SDCGNN$_{dk}$. The framework is primarily divided into three components: dividing, conquering, and fusing. Initially, crystal structural information is divided into crystal geometry (CG) and interstitial network (IN), which are performed graph representation. Then, two GNNs are constructed targeted for each based on their unique characteristics, with domain knowledge embedded in the modelling process, which aims to effectively conquer the divided crystal structural information (i.e., CG and IN). Finally, the structural representation vectors from different perspectives are fused to predict material properties.

Dataset construction

Building a high-quality graph dataset is essential for leveraging GNNs to establish accurate structure-activity relationships of ionic transport barriers in inorganic compounds. However, to the best of our knowledge, graph-based datasets for driving GNNs to explore the ion transport properties are still lacking. To address this gap, we adopt activation energy (i.e., the energy barrier that ions need to overcome when moving within the material [1]) as a breakthrough point for exploring the ion transport properties.

Concretely, we first collect a total of 125,223 Crystallographic Information Files (CIFs) spanning the years 1980-2025 from the Inorganic Crystal Structure Database (ICSD), including 12 potential mobile ions (Li^+, Na^+, Mg^{2+}, $Cu^{(2,3+)}$, Al^{3+}, Zn^{2+}, K^+, Ag^+, Ca^{2+}, F^-, and O^{2-}); Next, we conducted preliminary sorting and standardization of these CIFs, followed by systematic screening and refinement of candidate compounds. By eliminating crystal structures with incomplete information, mismatched ion types, or duplicate records, we ultimately select 18,410 high-quality CIFs to satisfy characterization and modeling requirements. Subsequently, using our previously developed CCNB method [11], which integrates Crystal structure Analysis by Voronoi Decomposition (CAVD) [22] and BVSE calculations, we extract the information on interstitial networks (including interstitial sites, transport channels, and threshold criteria for ion accessibility) and compute the corresponding ion migration energy barriers (namely activation energies) for each crystal structure. This process resulted in a comprehensive graph dataset capturing the ternary relationship among crystal structures, interstitial networks, and activation energies for 18,410 inorganic compounds across 12 mobile ion types, as summarized in Fig.2. Note that since this study aims to construct and validate models for exploring ion transport mechanisms in multi-system solid electrolytes, all models will be trained on the combined dataset encompassing all ion species.

From Fig.2, the number of crystalline materials with O^{2-} as the migrating ion is the highest, reaching 8,924 samples, detailed in Fig.2(a). This clearly suggests that oxygen-containing materials are predominant in the dataset of inorganic compounds investigated. This phenomenon is primarily attributed to the high abundance of oxygen in nature and the widespread existence of oxides across various inorganic materials, which leads to a significant quantitative abundance for crystal structures featuring O^{2-} as the migrating ion. Fig.2(c) presents the distribution of activation energy (E_a), or migration barriers, for inorganic compounds corresponding to different migrating ions, following the elemental scope outlined in Fig.2(b). Further details regarding the E_a distributions for different ionic species are available in **Fig.S1** in the Supplementary Information (SI). We present the full spectrum of E_a values to ensure the dataset is comprehensive and unbiased, which is essential for maintaining the integrity of our chemical space exploration. Importantly, the inclusion of materials with high E_a is critical for developing robust deep learning models, as these "negative examples" allow the algorithms to accurately learn structural features that inhibit ion migration. While high barriers are less relevant for practical ion conduction, our subsequent

analysis explicitly focuses on the low E_a subset for identifying promising materials.

It is noteworthy that the compounds with Li^+ as the migrating ion exhibit the lowest activation energy (indicated by the lowest median of the Li^+ distribution in Fig.2(c)), suggesting that Li^+ compounds possess outstanding ion transport properties. This characteristic can be attributed to the smaller ionic radius and lower mass of Li^+, which facilitates its rapid migration through interstitial channels in the crystal structure. In contrast, compounds with Ca^{2+} as the migrating ion generally exhibit significantly higher activation energy (with majority being above 1.0 eV; as shown in **Fig. S1**, the fraction of samples below 1.0 eV being merely 5.3%). This high barrier is primarily due to Ca^{2+} having both a high ionic charge (2+) and a larger ionic radius.

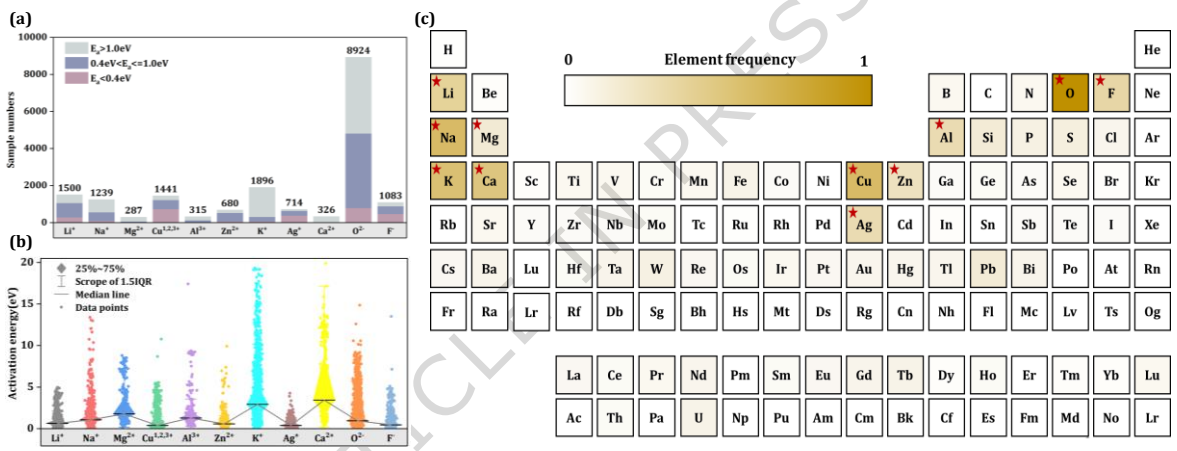

Fig.2. Statistical analysis of ionic transport performance within the dataset. (a) and (b) illustrate the distribution characteristics of transport barrier values categorized by migrating ions, while (c) presents the frequency distribution of each element across all inorganic compounds.

As for crystal structure graph representation, the atoms are set as nodes, with edges defined by interatomic interactions, such as chemical bonds or nearest-neighbor pairs, to reflect the topological arrangement of materials. To ensure node features capture the intrinsic physicochemical properties of each element, we initialize them using MEGNet pre-trained atomic feature vectors [17]. These vectors encapsulate critical Periodic Table data, including electronic configuration, electronegativity, and atomic radius. For edge construction, we employ radial basis function (RBF) to map interatomic distances into a high-dimensional space, which accounts for the continuous and nonlinear nature of spatial relationships, thereby enhancing sensitivity and generalization of models to geometric structural variations.

In contrast, the interstitial graph representation focuses on ion transport pathways. It defines unoccupied interstitial voids as nodes and establishes edges based on the minimum diffusion

bottlenecks between them. This representation captures the spatial connectivity and geometric constraints of ion migration channels. Interstitial node features incorporate geometric dimensions and the local coordination environment (including the species and distance distributions of nearest neighbors) to account for microscopic factors influencing ion-hosting capacity. Edge features prioritize bottleneck sizes and can integrate local potential barriers (site energies), explicitly modeling the spatial obstacles encountered during migration.

By capturing both atomic configuration and interstitial network topology, this dual-structure crystal graph provides a representation that is both information-rich and physically interpretable, laying a robust foundation for the downstream modeling of ion transport properties (details in Section of Dual-structure graph representation method that combines crystal geometry and interstitial network). The details of feature dimensions for both graph representations are provided in **Table S1** of SI.

Dual-structure graph representation method that combines crystal geometry and interstitial network

Typically, a crystal graph is defined as $\mathcal{g} = [v_i, e_{ij}, u]$ based on crystal structure, where v_i represents the atoms, e_{ij} represents the spatial distance between atoms i and j, u represents the global state feature. It has already achieved remarkably high accuracy for predicting material properties such formation energy (E_f) and band gap (E_g)[7], however, it still has a challenge in predicting ionic transport barriers in inorganic compounds. Crystal geometry can be described in terms of topological connectivity, which is commonly represented as a graph by treating atoms as nodes and chemical bonds as edges. This representation effectively captures the local chemical environment and topological characteristics of materials, making it well-suited for characterizing static structural properties. However, such a representation presents significant limitations in modeling dynamic ion transport processes, particularly due to its inability to accurately reflect actual ion migration pathways and the associated geometric constraints.

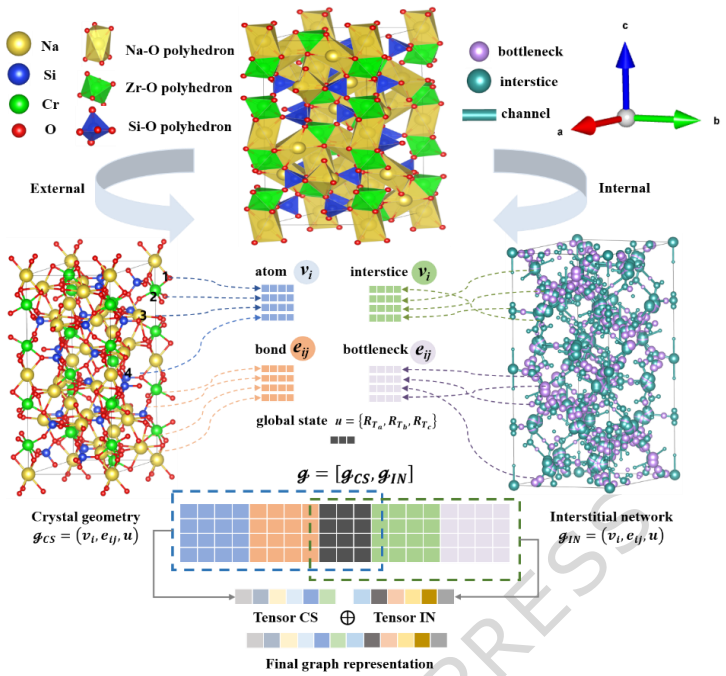

Fig.3. Overall framework of Dual-CGR. The crystal space is divided into two parts: crystal geometry and interstitial network. Crystal geometry is composed of atoms as nodes and interatomic bonds as edges to form a graph; Interstitial network is composed of interstitial sites as nodes and bottlenecks as edges to form a graph.

Hence, we propose a dual-structure graph representation method (Dual-CGR) combining crystal geometry and interstitial network, as shown in **Fig.3**. Concisely, the crystal structure is divided into two substructures: (1) crystal geometry (2) interstitial network. Therefore, crystal graph can be defined as $g = [g_{CS}, g_{IN}]$, with node and edge representations for g_{CS} and g_{IN}, respectively. In the crystal graph representations, the node initialization matrix R employs 16-dimensional pretrained features derived from MEGNet [17] via supervised learning on large-scale materials datasets, embedding rich physical/chemical information. Given the node set $V = \{v_1, v_2, \ldots v_n\}$, where $n = |V|$ denotes the number of atoms, the node feature matrix $R \in \mathbb{R}^{n\times 16}$ is defined as in Eq. (1):

$$R = \begin{bmatrix} r_1 \\ r_2 \\ \vdots \\ r_n \end{bmatrix}, r_i = [r_{i1}, r_{i2}, \cdots, r_{i,16}]^T \in \mathbb{R}^{16} \quad (1)$$

where r_{ij} represents the j-th component of the feature vector for atom i. initialization matrix facilitates the numerical integration of chemical and topological attributes into the GNN framework. For edge initialization, a Gaussian basis function-based distance expansion is employed as RBF, to capture geometric relationships between nodes and quantify their effects, which is defined in Eq. (2).

$$\varphi_k(r) = \exp\left[-\frac{(d_{ij} - d_k)^2}{\sigma^2}\right], \quad k = 1, 2, 3, \ldots, K \tag{2}$$

where d_{ij} denotes the distance between nodes *i* and *j*, d_k and σ represent the center of the k-th Gaussian basis function and the standard deviation controlling its width. Here, d_k are uniformly spaced over $[0, 8]$ with $K = 100$, covering the relevant distance range. The fixed $\sigma = 0.5$ ensures localized responses with moderate overlap, enhancing feature continuity and resolution. The Gaussian basis mapping transforms edge distance into *K*-dimensional vector, as shown in Eq. (3) :

$$e_{ij} = \left[\varphi_1(d_{ij}), \varphi_2(d_{ij}), \ldots \varphi_k(d_{ij})\right]^T \tag{3}$$

In the graph representation of IN, interstices are represented as nodes, characterizing unoccupied sites. For each interstice node v_i, its local chemical environment ξ_i, and size t_i are critical to ionic transport behavior. Therefore, each interstice node v_i is initialized by a multidimensional feature vector h_i. Especially, for a given interstice node v_i, its local chemical environment is described by the *k* nearest neighboring atoms $\{a_1, a_2, a_3, \cdots, a_k\}$ within a radius of *m* Å. Here, we set *m* and *k* as 8 and 12, respectively. Each atom a_j is associated with an intrinsic property vector $p_j \in \mathbb{R}^k$ (e.g., atomic number, density, molar volume, and other physicochemical characteristics) and its distance to the interstice node r_{ij}, as shown in Eq. (4):

$$\xi_i = Concat\left(\sum_{j=1}^{k} p_j, r_{ij}\right) \tag{4}$$

where $Concat(\cdot)$ denotes the concatenation operation, which integrates the intrinsic property vector p_j of each neighboring atom with its corresponding distance r_{ij} into a unified representation. The complete feature vector of interstice node v_i comprises its size t_i and the encoded local chemical environment ξ_i, as formulated in Eq. (5):

$$h_i = Concat(\xi_i, t_i) \tag{5}$$

In addition, the edge representations (i.e., bottlenecks) are initialized based on their geometric dimensions. Let e_{ij} denote the bottleneck connecting two interstice nodes v_i and v_j. The bottleneck corresponds to the narrowest region between them, characterized by a dimension b_{ij}. The ion's ability to migrate through this bottleneck is constrained by the relative size b_{ij} with

respect to the ion's effective radius r_{ion}, making the bottleneck dimension a critical determinant of ion accessibility. Specifically, the accessible range is defined by a lower and upper threshold, T_1 and T_2, respectively, as shown in Eq. (6):

$$T_1 = \alpha \cdot r_{ion}, T_2 = \beta \cdot r_{ion} \tag{6}$$

where $\alpha = 0.8$ and $\beta = 1.2$. Ion migration between adjacent interstice v_i and v_j is considered feasible if the bottleneck dimension satisfies $T_1 \leq b_{ij} \leq T_2$. To further characterize the material's overall ion transport capability, we introduce the conduction threshold vector $R_T = \{R_{T_a}, R_{T_b}, R_{T_c}\}$ as a global feature u. E_d denotes the set of edges along the crystallographic direction d. R_{T_a}, R_{T_b} and R_{T_c} denote the minimum bottleneck sizes along the primary crystallographic directions a, b, c. the conduction threshold R_{T_d} is defined as Eq. (7):

$$R_{T_d} = min\{(b_{ij}|(i,j) \in E_d)\} \tag{7}$$

Incorporating domain knowledge into the GNN modelling process

GNNs directly work on graph-structured data and have strong ties to the field of geometric deep learning [7]. Most GNNs designed for materials science can be summarized under the framework of Message Passing Neural Networks (MPNNs) as suggested by Gilmer et al. [23] To ensure the capture of valuable information of ionic transport process latent in graph-structured data, we here propose an attention mechanism that incorporates materials domain knowledge into the message passing stage of MPNN. Specifically, the proposed mechanism comprises local and global attention layers, where the attention coefficients λ_{ij} are computed using both data-driven and knowledge-driven coefficients, i.e., $e_{ij-data}$ and e_{ij-dk}, as shown in Eq. (8) - (11).

$$\lambda_{ij} = softmax(e_{ij}) = \frac{exp(e_{ij})}{\sum_{j \in N_i} exp(e_{ij})} \tag{8}$$

$$e_{ij} = e_{ij-data} + e_{ij-dk} \tag{9}$$

$$e_{ij-data} = a_{data}^T [W^h v_i^{h-1} \oplus W^h v_j^{h-1}] \tag{10}$$

$$e_{ij-dk} = a_{dk}^T W^h [\Delta E_{ij} \oplus R_{ij}] \tag{11}$$

where a_{data}^T and a_{dk}^T is learnable weight vector. W means the weight matrix of layer h, while

v and $\oplus$ define a node feature vector and the concatenation operation. N_i is the set of neighbors of node i. The energy difference $\Delta E_{ij} = \left|E_{void_i} - E_{bottleneck_{ij}}\right|$, which means the energy barrier for ions to migrate from void i to j. E_{void} and $E_{bottleneck}$ are calculated by Eq.(12) and Eq.(13). R_{ij} defines the bottleneck radius between void i and j.

$$BVSE(M) = \frac{D_0}{2}\sum_i \{(exp[\alpha(R_{min} - R)] - 1)^2 - 1\} + \sum_{i=1}^{N} E_{Coulomb}(M - M_i) \tag{12}$$

$$E_{coulomb}(M_1 - M_2) = \frac{q_{M_1} q_{M_2}}{R_{M_1 - M_2}} erfc\left(\frac{R_{M_1 - M_2}}{\rho_{M_1 - M_2}}\right) \tag{13}$$

where D_0, α, R_{min} are Morse potential parameters are empirical constants determined from experimental crystal structural data for a large number of stable compounds. $R_{M_1-M_2}$ is the distance between ion M_1 and M_2. q is the effective charge carried by the ion, the screening factor $\rho_{M_1-M_2} = 0.74 \times \left(r_{M_1} + r_{M_2}\right)$.

Note that departing from the BVSE calculation approach in CCNB, which involves massive redundant sampling across the global crystal space (typically encompassing millions of points), we instead focus on key energy-relevant sampling sites, such as interstitial sites and migration channel bottlenecks. Specifically, we only calculate the interatomic interactions between each target site and its nearest neighboring atoms within a 10 Å cutoff radius, resulting in a total of merely thousands of sampling sites (only a tiny fraction of the number of computational sites of BVSE calculation). It is important to emphasize that these descriptors capture "local" environmental potentials rather than the "global" migration barrier itself. Since the target label (E_a) is the result of a complex path-finding process across the entire potential energy surface, providing these discrete local energy points acts as a physical prior, rather than a direct injection of the label. This approach not only overcomes the efficiency limitations of conventional methods but also provides models with highly condensed, valid domain knowledge.

Then, to stabilize the learning process of self-attention, we employ multi-head attention mechanisms. The node feature vector v_i^h is updated by the following convolution in Eq. (14):

$$v_i^h = \sigma\left(\frac{1}{K}\sum_{k=1}^{K}\sum_{j\in N_i}\lambda_{ij}^k W^k v_j^{h-1}\right) \tag{14}$$

where K and λ_{ij}^k defines the number of attention heads and attention coefficient at the kth attention head, σ is the nonlinear activation function. In addition, we also focus on the global attention coefficients and propose a global attention layer that integrates $R_T = \{R_{T_a}, R_{T_b}, R_{T_c}\}$, which can be implemented by Eq. (15) and Eq. (16). R_T, as global state u, participates in the calculation of global attention coefficient e_i^u with node feature vectors v_i. Each e_i^u is normalized by the $softmax$function and the normalized global attention coefficient λ_i^u is obtained. Then, λ_i^u is multiplied by the corresponding feature vector v_i and the final graph representation vector G are obtained by aggregating the information of all nodes and λ_i^u, which are shown in Eq. (17).

$$e_i^u = W\big(\sigma(v_i \oplus R_T)\big) \tag{15}$$

$$\lambda_i^u = softmax(e_i^u) = \frac{exp(e_i^u)}{\sum_{i\in\mathcal{g}(i)} exp(e_i^u)} \tag{16}$$

$$G = \sum_{i\in\mathcal{g}(i)} \lambda_i^u v_i \tag{17}$$

We used the GNN architecture proposed by Chen et al [17] to learn the structure representation of $\mathcal{g}_{CS}$. Domain knowledge is incorporated into the MEGNet-Block to further improve accuracy for the mining of ionic transport features. Concisely, $R_T = \{R_{T_a}, R_{T_b}, R_{T_c}\}$, as the global state, is introduced to the message function of MEGNet-Block to update node, edge, and global state features of $\mathcal{g}_{CS}$.

A hybrid-level feature fusion strategy (FFS) based on structural importance

G_{cs} and G_{IN} are the structure representation vectors of crystal structure and interstitial network, respectively. Then feature fusion should be performed to obtain a complete representation vector. To our best of knowledge, there is no research to discuss the structural feature fusion method in materials science. In this work, we design a series of feature fusion strategies, which are summarized in **Table 1**. Fusion strategies of feature level, decision level, hybrid level, and model level significantly improve the prediction performance of barriers and FFS-2 achieves the

highest coefficient of determination. FFS-1 is intuitive and easy to train but susceptible to the influence of irrelevant features. FFS-2 can adaptively learn the weights of G_{cs} and G_{IN} via the $softmax$ function and filter out the redundant features. FFS-3 takes the diversity of FFS-1 and FFS-2 into account at the expense of computing cost and interpretability. FFS-4 is implemented based on Long Short-Term Memory (LSTM), which is the most complex feature fusion strategy among them. Employing LSTM as the main architecture of FFS-4 makes the GNN model too complex, which not only reduces the interpretability and generalization, but also decreases the prediction accuracy.

Table 1. Five feature fusion strategies (FFS)

Feature vector fusion	Fusion level	Feature Formulation	Method Identifier
Concatenate G_{cs} and G_{IN}	Feature level	$\mathrm{G} = \sigma\left(W(G_{cs} \oplus G_{IN})\right)$	FFS-1
Get the decision results of G_{cs} and G_{IN}	decision level	$a_{CS} = WG_{CS}, a_{IN} = WG_{IN}$ $\mathrm{G} = W(a_{CS} \oplus a_{IN})$	FFS-2
Concatenate G_{cs} and G_{IN} and their labels	hybrid level	$a_{CS}, a_{IN} = (WG_{CS}, WG_{IN})$ $\mathrm{G} = \sigma\left(W(G_{cs} \oplus a_{CS} \oplus G_{IN} \oplus a_{IN})\right)$	FFS-3
Based on multi-layers LSTM	model level	$\mathrm{G} = \sigma\left(W\left(LSTM\left(G_{cs} + LSTM(G_{IN})\right)\right)\right)$	FFS-4
Get the weight of G_{cs} and G_{IN}	hybrid level	$w_{CS}, w_{IN} = softmax(WG_{CS}, WG_{IN})$ $\mathrm{G} = \sigma\left(W(a_{CS}G_{cs} \oplus a_{IN}G_{IN})\right)$	FFS-5

We further employ FFS-5 due to the consideration of model efficiency and interpretability and proposed a feature fusion strategy based on structural importance. FFS-5 assigns a weight coefficient for each structure representation (i.e., w_{CS} for the representation of crystal structure and w_{IN} for the representation interstitial network) and fully integrates the information of two microstructures to obtain the final spatial structure representation vector.

Model evaluation

Table 2 presents the average results of our method in comparison to conventional graph neural network architectures across these ten experiments (including standard deviation). The results demonstrate that our model achieves superior prediction accuracy for activation energy, with an average increase of 30% in the R^2 metrics. Furthermore, the experimental findings indicate that reliance solely on crystal structure information for modeling fails to adequately capture the complexities of ionic transport, resulting in diminished predictive accuracy for activation energy. Our research not only incorporates the crystal structure but also integrates information on the interstitial network that characterizes ionic transport pathways, alongside relevant domain

knowledge, to construct both graph neural network models and their fused variants. This approach facilitates a more comprehensive and precise exploration of the structure-activity relationships associated with ionic transport within the crystalline matrix. Moreover, the performances of different models for each transport ion are shown in **Table. S1**. To highlight the predictive performance of different models for ion transport, we here take Ca-containing ionic compounds as an example: For E_a prediction of Ca-containing ionic compounds (Ca^{2+}), $SDCGNN_{dk}$ achieves an R^2 of 0.9300, which is a ~58% improvement over the second-best model (BNMCDGNN , R^2=0.3464). Meanwhile, its RMSE is 64.8% lower than that of CGCNN (3.3251 eV). This accuracy enhancement highlights stronger capability of $SDCGNN_{dk}$ to capture the migration features of high-charge-state ions. The performance gain is practically meaningful for electrolyte material screening: the MAE of $SDCGNN_{dk}$ (0.6755 eV) is far lower than that of the classical GNN, MEGNet, (2.3750 eV), implying a ~72% decrease in misjudgment probability when selecting high-mobility electrolytes. This can substantially reduce the cost of subsequent experimental validation. The failed fitting of CGCNN for Ca^{2+}, of which R^2 values are less than 0, stems from its isotropic message-passing scheme, which simplifies the chemical environment into a collection of pairwise distances, while Ca^{2+} migration involves long-range lattice distortion, a dynamic, long-range structural change that exceeds feature-capturing scope of CGCNN. Moreover, GATGNN, SLIGNN, MEGNet and BNMCDGNN show poor performance for Ca^{2+}, which may be because these models primarily rely on local atomic environment embeddings while neglecting large-scale structural evolution caused by long-range distortions. In such cases, the noise captured by the models far exceeds the signal, leading to a complete breakdown in prediction accuracy. Notably, although O^{2-} containing entries constitute the majority of the dataset, they do not dominate the decision-making process of $SDCGNN_{dk}$ or compromise its predictive accuracy for other species. This robustness against data imbalance is primarily attributed to the fine-grained physical encoding within our $SDCGNN_{dk}$ architecture. As detailed in **Table S1**, instead of relying solely on crystal structure information, our model integrates the information of IN that describes carrier-specific local environments. The high-dimensional interstice features describe the intricate chemical and geometric surroundings, while the bottleneck features provide critical constraints on site energy and transition-state geometry. This path-specific representation ensures that the input features for different ions remain physically distinct and highly informative. Consequently, as evidenced by the consistent high performance across all ion types in **Table S2**, the model successfully learns

universal physical principles governing ion transport rather than superficial statistical correlations. This underscores the scientific utility of our approach in providing reliable, carrier-specific migration barrier predictions regardless of the underlying sample distribution. This illustrates that the dual graph representation mechanism embedded with materials domain knowledge of $SDCGNN_{dk}$ is tailored to model such dynamic migration trajectories, explaining its consistent superiority.

Table 2. Comparison of the R^2, RMSE, MAE in the activation energy (E_a) between $SDCGNN_{dk}$ and prior works on the self-constructed dataset.

Model	R^2 of E_a		MAE of E_a (eV)		RMSE of E_a (eV)	
	Ave.	Std.	Ave.	Std.	Ave.	Std.
CGCNN [16]	0.5235	0.0296	0.5212	0.0239	1.3526	0.0746
MEGNet [17]	0.6252	0.0312	0.4653	0.0186	1.1988	0.0655
GATGNN [19]	0.5927	0.0289	0.4852	0.0148	1.2496	0.0549
GeoCGNN [18]	/	/	2.9244	3.5957	108.3066	153.5370
SLI-GNN [20]	0.5007	0.0745	0.5850	0.0486	1.3582	0.1203
BNM-CDGNN [21]	0.6645	0.0463	0.4293	0.0221	1.0977	0.0702
$SDCGNN_{dk}$	**0.9130**	**0.0074**	**0.2546**	**0.0073**	**0.5687**	**0.0354**

* "Ave." means the average of prediction performance of models; "Std." means the standard deviation of prediction performance of models; "/" means this model has not converged well.

A comparative analysis of model prediction accuracy under various feature fusion strategies is shown in **Fig.4.(a)**. The results indicate that the decision-level feature fusion strategy achieves the highest predictive performance. While both feature-level and mixed-level strategies yield results comparable to those of the decision-level strategy, they nonetheless fall short of its level of accuracy, with the model-level strategy exhibiting the lowest predictive capability. The feature-level fusion strategy is inherently simplistic, directly merging feature vectors from disparate perspectives. Although this streamlining of processing may enhance efficiency, it may not fully leverage the information provided by each perspective. In contrast, the decision-level strategy independently computes the decision coefficients for each perspective, thereby allowing for more nuanced information integration. The mixed-level strategy seeks to combine the strengths of both decision-level and feature-level approaches. The model-level strategy employs LSTM to extract features from a singular perspective; however, the resultant complexity of the model may contribute to a reduction in predictive accuracy. Thus, the judicious selection of feature fusion strategies is paramount for optimizing model performance. In light of considerations regarding model interpretability and predictive precision, we ultimately opt for the decision-level fusion strategy as our methodological approach. **Fig.4.(b)** illustrates the error reduction curve of the model during the training process. It is evident that the model converges around the $100th$ epoch,

indicating that the loss function decreases rapidly and stabilizes throughout the training. This rate of convergence suggests that our model can effectively capture the underlying patterns in the data and quickly adapt to changes in the input features. Furthermore, the early convergence implies the model's efficiency and effectiveness in handling the task, thereby effectively reducing the risk of overfitting. **Fig.4.(c)** presents the correlation analysis between the predicted values of activation energy (E_a) for surface reactions over multicomponent catalysts from the SDCGNN$_{dk}$ model, and the results from BVSE calculations. In terms of sample point distribution, all pink scatter points corresponding to the data are closely clustered around the reference line. This analysis aims to assess the reliability of the model in replacing BVSE calculations to enable rapid prediction of E_a.

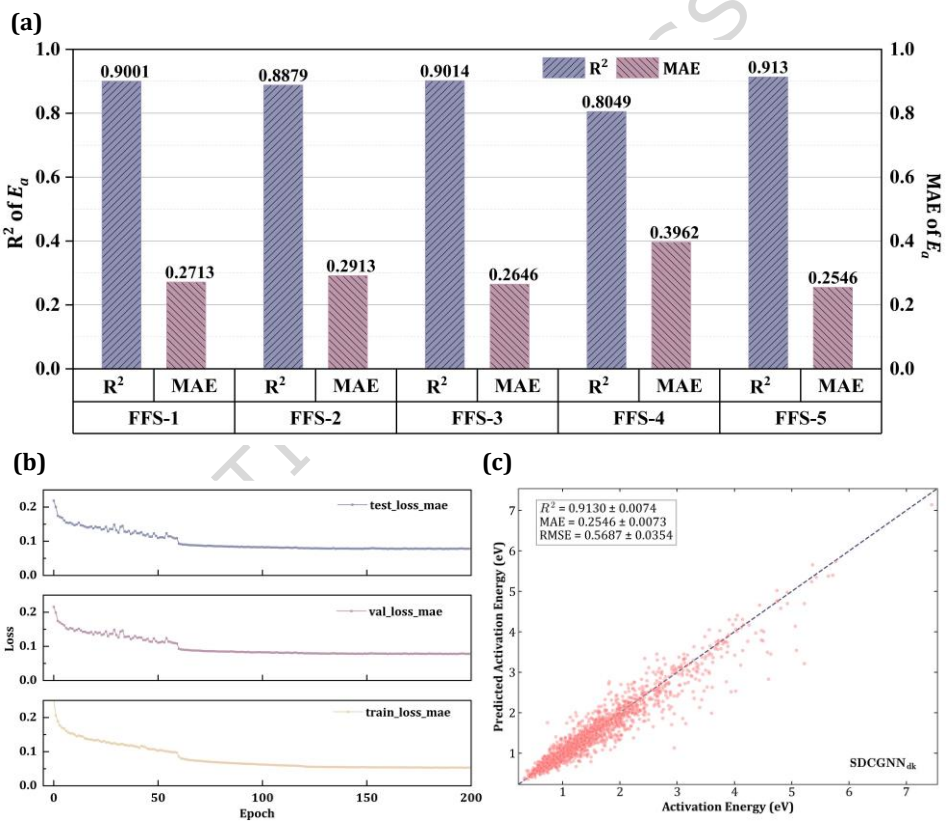

Fig.4. The average performance of different models in predicting E_a for multi-system solid electrolyte. (a) the comparison of 4 different feature fusion strategies; (b) the average loss curve of model training process; (c) the scatter plot of the activation energy prediction results.

Ablation study

To verify whether integrating materials domain knowledge is a key factor in boosting the predictive performance of the SDCGNN$_{dk}$ model, this section carries out a set of hierarchical ablation experiments. By incrementally incorporating distinct domain knowledge modules (as

defined in the study), five model variants ($SDCGNN_{dk}$-0 to $SDCGNN_{dk}$-4) are constructed. Their performance on the ion transport property prediction task is evaluated using two metrics, i.e., R^2 and MAE. Specifically, $SDCGNN_{dk}$-0 serves as the baseline, which only adopts the structure divide-and-conquer strategy, without integrating any of the three target domain knowledge modules (pre-trained elemental embeddings, energy-difference, and global state features); $SDCGNN_{dk}$-1 enhances the baseline by adding pre-trained node features and atomic intrinsic attributes; $SDCGNN_{dk}$-2 builds on $SDCGNN_{dk}$-1 by further integrating site energy information (i.e., energy difference) derived from the CCNB method [11] into the attention mechanism. $SDCGNN_{dk}$-3 is based on $SDCGNN_{dk}$-1 but replaces the energy difference module with the global state module; $SDCGNN_{dk}$-4 combines all three domain knowledge modules (pre-trained elemental embeddings, energy-difference, and global state) on the basis of the baseline strategy. **Table 3** summarizes the average predictive performance of these $SDCGNN_{dk}$ variants under different domain knowledge integration configurations.

Table 3. Average model prediction performance under different domain knowledge embedded modules

Model	Domain knowledge			R^2 of E_a	MAE of E_a (eV)
	Pre-trained elemental embeddings	Energy difference	Global state $R_T = \{R_{T_a}, R_{T_b}, R_{T_c}\}$		
$SDCGNN_{dk}$-0	×	×	×	0.8063	0.3428
$SDCGNN_{dk}$-1	√	×	×	0.8279	0.3204
$SDCGNN_{dk}$-2	√	√	×	0.8448	0.3056
$SDCGNN_{dk}$-3	√	×	√	0.9018	0.2727
$SDCGNN_{dk}$-4	√	√	√	0.9130	0.2546

To visually capture the performance trend associated with incremental domain knowledge integration, we present an ablation trend plot, as shown in **Fig.5.**. In conjunction with the results from **Table 2**, **Table 3** and **Fig.5.**, it can be observed that even without any embedded domain knowledge, the $SDCGNN_{dk}$-0 model, based solely on the structure divide-and-conquer strategy, has already surpassed 6 other GNN models constructed using only crystal geometry. This finding further underscores the effectiveness of incorporating information on the interstitial network in capturing ion transport mechanisms.

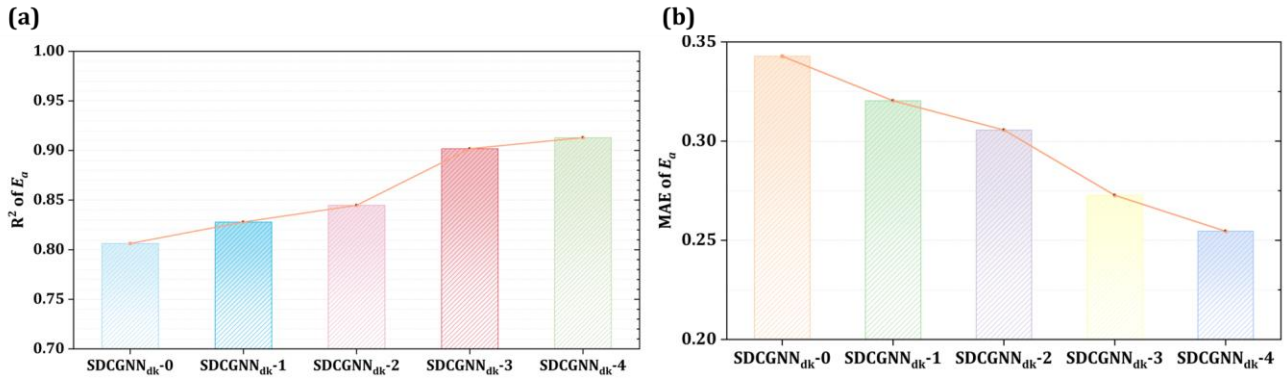

Fig.5. Results of the ablation experiments conducted on the model. (a) and (b) present the outcomes based on the R^2 and MAE metrics of E_a, respectively.

Specifically, SDCGNN$_{dk}$-1 replaces the One-Hot encoding (adopted by SDCGNN$_{dk}$-0) with physicochemical property vectors for node representation by integrating pre-trained elemental embeddings (atomic features and intrinsic properties). This adjustment enhances the E_a prediction performance: the coefficient of determination R^2 increases by ~2.2% (from 0.8063 of SDCGNN$_{dk}$-0 to 0.8279 of SDCGNN$_{dk}$-1). The improvement stems from the model's strengthened ability to capture local interactions via these pre-trained embeddings. Unlike One-Hot vectors (which only encode basic attributes like atomic numbers), pre-trained elemental embeddings encapsulate key physicochemical properties (e.g., atomic radius, electron configuration, electronegativity), filling the information gap of simple One-Hot encoding. SDCGNN$_{dk}$-2 further boosts performance by incorporating energy-difference features (calculated via the CCNB method) and integrating them as attention coefficients into the weight computation of the local attention layer. This leads to an R^2 increase from 0.8279 (SDCGNN$_{dk}$-1) to 0.8448, paired with an MAE reduction from 0.3204 to 0.3056. These energy differences (derived from BVSE calculations) quantify inter-node interaction strength, enabling the model to better identify critical "bottleneck nodes" and "high-energy-barrier passages". This optimization refines information propagation in the graph structure, thereby enhancing the model's ability to capture ion transport characteristics. SDCGNN$_{dk}$-3 embeds the global state feature $R_T = \{R_{T_a}, R_{T_b}, R_{T_c}\}$ (conduction threshold) to characterize the connectivity of macroscopic transport channels, which reflects whether continuous low-energy-barrier transport paths exist in the material, bearing clear physical significance. With this embedding, the model's R^2 rises to 0.9018 and MAE drops to 0.2727; compared to SDCGNN$_{dk}$-1, this corresponds to an R^2 improvement of ~5.7%. Finally, SDCGNN$_{dk}$-4 integrates all three types of materials domain knowledge (pre-trained elemental embeddings,

energy-difference, and global state R_T), each with clear physical significance. This leads to an R^2 of 0.9130 and an MAE of 0.2546, representing an ~10.7% R^2 improvement relative to $SDCGNN_{dk}$-0.

It is noteworthy that current research on material performance prediction remains largely confined to local structural modeling, with limited attention to global factors. This study illustrates that the approach of embedding a small portion of readily accessible intermediate outputs from complex computational methods (e.g., the CCNB method) into the process of model construction (e.g., the energy difference for attention matrix of local attention layer, conduction threshold for global embedding features), serves as a key entry point for integrating domain knowledge. This pathway is not only core to enhancing model generalization and accuracy, thereby refining the model's ability to capture structure-property relationships, but can drastically speed up the calculation of activation energy (from tens of minutes reduced to a few seconds).

DISCUSSION

The structure of materials directly determines their properties. Many isostructural compounds crystallizing in the same space group exhibit similar properties. Therefore, we conduct a statistical analysis of the space groups of materials with E_a below 1.2 eV, as presented in **Fig.S2** in **SI**. The results indicate that the space groups of these low-activation-energy materials are typically associated with Na Super Ionic Conductor (NASICON)-type compounds, such as $R\bar{3}c$, $P2_1/c$, $C2/c$. To identify relevant candidates, structural screening of the dataset is performed based on the chemical formula and space group information of the materials, leading to the selection of a set of NASICON-type materials for further analysis. The space groups of these selected materials not only include those corresponding to the intrinsic structural features of the NASICON family but also encompass space groups associated with phase transitions and those exhibiting analogous structural characteristics.

NASICON-type solid electrolytes hold great application potential in energy storage systems. These compounds are remarkably stable, as corner-sharing transition metal-oxide octahedra and phosphate tetrahedra form a robust 3-dimensional (3D) framework. This structural arrangement creates wide ion transport pathways, thereby enabling high ionic conductivity. Our material dataset contains 370 compounds that match the chemical formula of NASICON-type materials. Following

data cleaning and space group filtering, 5 compounds with an E_a below 1.0 eV are selected for detailed investigation.

As shown in **Table 4**, SDCGNN$_{dk}$ provides highly accurate predictions of E_a for NASICON-type solid-state electrolytes. Among the NASICON-type materials, in addition to the commonly observed space group $R\bar{3}c$, several other space groups are also present. For instance, $Th_2Cu(PO_4)_3$ exhibits the space group C2/c [24], $Li_3Fe_2(PO_4)_3$ adopts the space group *P2_1/c*, and $Li_3Sn_2(PO_4)_3$ is characterized by the space group P_1 [25], all of which feature the same corner-sharing NASICON-type framework. In addition, these low E_a materials also have the potential to become interface buffer layers for all-solid-state batteries. For example, $LiZr_2(PO_4)_3$ has relatively high oxidation stability (>5V) and excellent ionic conductivity ($10^{-5} - 10^{-4}\ S \cdot cm^{-1}$ at room temperature) and Wang et al. [26] used $LiZr_2(PO_4)_3$ as a buffer layer for the LCO ($LiCoO_2$)$/LPSCl$ (Li_6PS_5Cl) interface. First principles calculations and analysis showed that the activation energy of lithium-ion migration at the $LCO/LZPO$ and $LZPO/LPSCl$ interfaces decreased from 1.367 eV to 0.531 eV and 0.904 eV, respectively, while improving interface stability.

Table 4. Prediction of NASICON-type materials

Material id	Chemical formula	Space group	Cell volume	BVSE E_a (eV)	Predicted E_a (eV)
ICSD_80863	$Th_2Cu(PO_4)_3$	C2/c	988.2904	0.2832	0.3253
ICSD_60948	$Li_3In_2(PO_4)_3$	P2_1/c	940.6463	0.5859	0.5428
ICSD_96964	$LiV_2(PO_4)_3$	P2_1/c	823.8331	0.6543	0.6837
ICSD_96963	$Li_2V_2(PO_4)_3$	P2_1/c	867.2383	0.4785	0.4536
ICSD_201935	$LiZr_2(PO_4)_3$	R-3c	1507.5005	0.3906	0.3724

Building upon the structure-importance-based hybrid-level feature fusion strategy proposed in Section of A hybrid-level feature fusion strategy (FFS) based on structural importance, two weighting parameters (i.e., $\boldsymbol{w_{IN}}$ and $\boldsymbol{w_{cs}}$) of the features from GNNs for interstitial network and crystal structure in the final fusion vector, output by FFS-5 are extracted to systematically quantify the relative contributions of structural features from different perspectives to the target property. Based on the dataset constructed in Section of Dataset construction, structural importance analysis reveals that approximately 67% of the compounds exhibit ion transport performance predictions that rely more heavily on the interstitial network, whereas the remaining 33% are predominantly influenced by the crystal structure. This distribution pattern highlights that, for the complex system of solid-state electrolytes, the interstitial network generally constitutes the dominant structural

subgraph governing ionic transport behavior. Furthermore, 9 representative compounds are selected to investigate the structure-activity relationships between their structural features and ion transport performance, as summarized in **Table 5**.

We find that for compounds with complex structures and high percolation thresholds, ion migration pathways typically exhibit dense bottleneck distributions, coexistence of multiple channels, and pronounced topological branching. In such cases, predictive performance relies predominantly on the interstitial network. For example, in $ZnCr_2O_4$ (ICSD_171898), the crystal graph contains 93 atomic nodes, whereas the interstitial network comprises 207 interstitial nodes and 896 bottleneck points, indicating intricate topology. Here, model prediction is almost entirely dependent on the interstitial network, underscoring the critical roles of structural redundancy and bottleneck density in ion transport. In contrast, for compounds with ordered structures, well-defined migration pathways, and continuous channels, predictive performance is primarily governed by the crystal structure. For instance, Li_2O (ICSD_173193) features a crystal graph with only 21 atomic nodes and an interstitial network comprising 12 nodes and 63 bottleneck points. In such systems, ion transport behavior is largely dictated by the stability and configurational order of the crystal framework.

Table 5. Structural characteristics of various inorganic compounds and the FFS-5 predictions of their $\boldsymbol{E_a}$.

ID	Interstitial network	w_{IN}	Crystal geometry	w_{cs}	R_T	BVSE E_a (eV)	Predicted E_a (eV)
ICSD 171898	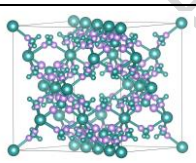	0.85	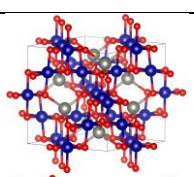	0.15	0.7122	0.4689	0.5002
ICSD 155635	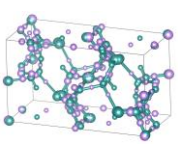	0.71	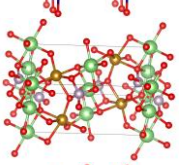	0.19	0.4226	0.3809	0.4391
ICSD 18096	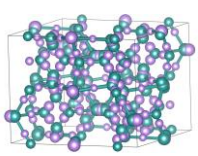	0.66	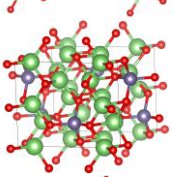	0.34	0.6201	0.5371	0.4956
ICSD 181312	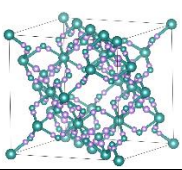	0.81	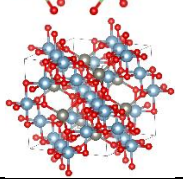	0.19	0.6005	0.4981	0.5131

ICSD 628110	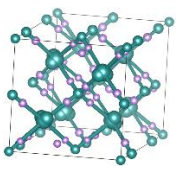	0.79	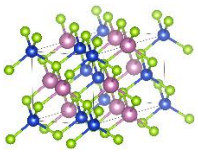	0.21	0.5485	0.4297	0.4947
ICSD 52232	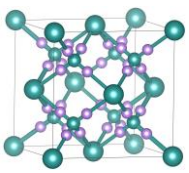	0.17	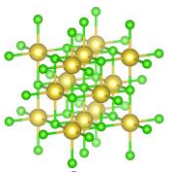	0.83	0.6321	0.8105	0.8356
ICSD 44781	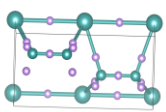	0.23	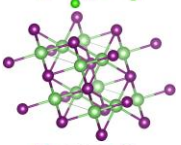	0.77	0.5176	0.2832	0.3027
ICSD 173193	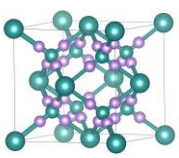	0.34	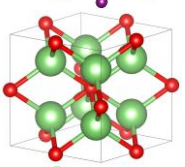	0.66	0.61	0.3027	0.2687
ICSD 56541	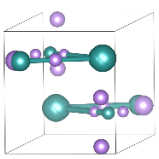	0.37	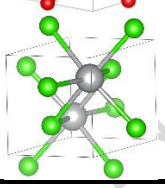	0.63	0.5439	0.4687	0.4055

*"$\boldsymbol{w_{IN}}$" and "$\boldsymbol{w_{cs}}$" means the weight ratio of the features from GNN for interstitial network and crystal structure in the final fusion vector.

These findings are corroborated by expert insights from the research team: when the crystal structure is regular and the ion migration space is continuous and open, the crystal framework alone sufficiently captures the migration mechanism. Conversely, in systems with complex configurations and branched topologies, ion migration exhibits heterogeneous bottleneck and channel distributions, with the interstitial network providing a more sensitive depiction of pathway connectivity and blockages. This reveals a fundamental principle: neither crystal geometry nor interstitial network is an exclusive factor but instead they exhibit a complementary and synergistic relationship in governing ion transport. The crystal framework establishes the initial energy landscape and geometric boundaries of migration, while the interstitial network modulates pathway extensibility, bottleneck distributions, and spatial connectivity. Their interplay underpins the intrinsic transport mechanisms.

In conclusion, we develop a structure divide-and-conquer graph neural network framework for unveiling structure-activity relationships of transport barriers by incorporating domain knowledge, which marks an advanced development of the divide-and-conquer modeling strategy [27]. Our method outperforms the conventional GNNs that are only based on crystal geometry

information by over 10% on average. This significant improvement demonstrates that dual-structure crystal graph representation and incorporating materials domain knowledge into the GNN modeling process can significantly improve the model performance in predicting ionic transport barriers. Ablation studies further verify the effectiveness of incremental addition of domain knowledge consistently enhances the prediction performance of GNNs. Meanwhile, through quantifying the importance of crystal geometry and interstitial network to the ionic transport property, our approach provides an insight for researchers to understand the ion transport structure-activity relationships between the microstructure and ionic transport barriers. It is worth noting that existing studies, including the present work, primarily focus on ordered crystal structures. In future research, we aim to extend our scope to disordered systems by leveraging robust approaches for modeling site-occupancy disorder, e.g., MCTSGT method [28] that efficiently identifies representative configurations of site-occupancy disorder through Monte Carlo Tree Search and graph-theory-based pruning. Overall, our work provides a new research perspective and method for comprehensively unveiling the structure-activity relationship of ion transport barriers, which can promote the design and discovery of new advanced ionic conductors.

METHOD

Message passing neural network

The Message Passing Neural Network [23] is a deep learning architecture designed for implementation in materials science and chemistry. They were introduced as a framework to generalize several proposed techniques [29-31], and have demonstrated state-of-the-art results on multiple related benchmarks. MPNNs contain three major operations: message passing, node update, and readout. At the very beginning, each node in the graph is assigned with an initial state v_i^0. Then, each node updates its own state by aggregating information from its immediate neighborhood. This is done according to the following formulas:

$$m_v^t = \sum_{j \in N(V)} M_t\left(v_i^t, v_j^t, e_{ij}\right) \tag{18}$$

$$v_i^{t+1} = U_t(v_i^t, m_v^t) \tag{19}$$

where M_t is the message function, U_t is the node update function, v_i^t is the hidden state of node v at time t, e_{ij} is the hidden state of edge between node v and j, $N(V)$ is the set of neighbors

of node v, and m_v^t is a corresponding message vector. After a chosen number of "messaging rounds", all these context-aware node states are collected and converted to a summary representing the whole graph. This process is shown in Eq. (20):

$$\hat{y} = R(\{v_i^K | i \in G\}) \tag{20}$$

Where $\hat{y}$ is the feature vector representing the whole graph, R is the readout function.

Attention Mechanism

Attention mechanisms have been widely used in various tasks of deep learning, such as computer vision (CV), natural language processing (NLP) and speech recognition (SR) [32-34]. The rise of diverse graph data types such as social networks, knowledge graphs, and recommendation systems underscores the growing significance of attention mechanisms in graph analysis. Conventional GNNs regard each node as a static entity, often overlooking its position within the graph or its interrelations with other nodes. The incorporation of attention mechanisms empowers GNNs to dynamically allocate focus to varying nodes or edges during graph convolution, thereby enhancing the capture of both local and global structural features within the graph.

Attention mechanisms are also applicable to research in materials science, offering a means to analyze the crystal structure and predict properties through the utilization of both local and global attention mechanisms. Local attention primarily directs focus towards the localized chemical environments within the crystal structure, with the aim of accurately simulating atom interactions and identifying structural characteristics. Global attention encompasses the contributions of each atom to the entirety of the crystal structure. By synergistically employing both local and global attention mechanisms, the precision of crystal structure analysis and property prediction can be heightened.

MEGNet Block

MEGNet is a general message passing framework for crystals proposed by Chen et al. [17]. In MEGNet, a crystal graph can be defined as $G = (V, E, u)$. MEGNet block provides a universal update operation for nodes, bond and global state. The feature vectors of each bond are updated using feature vectors from itself, its connecting atoms v_i and v_j and global state vector u, as follows:

$$e'_{ij} = \phi_e\left(v_i \oplus v_j \oplus e_{ij} \oplus u\right) \tag{21}$$

where ϕ_e is the bond update function and $\oplus$ is the concatenation operator Next, the feature vectors of each atom are updated using feature vectors from itself, the bonds connecting to it, and the global state vector u, as follows:

$$\bar{v}_i^e = \frac{1}{N_i^e}\sum_{j=1}^{N_i^e} e'_{ij} \tag{22}$$

$$v'_i = \phi_v(v_i \oplus u \oplus \bar{v}_i^e) \tag{23}$$

where N_i^e is the number of bonds connecting to atom i and ϕ_v is the atom update function. The aggregation step acts as a local pooling operation that takes the average of bonds that connect to the atom i. The global state vector u is updated using information from itself and all atoms and bonds, as follows:

$$\bar{u}^e = \frac{1}{N^e}\sum_{j=1}^{N^e} e'_{ij} \tag{24}$$

$$\bar{u}^v = \frac{1}{N^v}\sum_{i=1}^{N^v} v'_i \tag{25}$$

$$u' = \phi_u(\bar{u}^e \oplus \bar{u}^v \oplus u) \tag{26}$$

where ϕ_u is the global state update function. MEGNet block also contains residual netlike skip connections to enable deeper model training and reduce over-fitting.

Evaluation metrics

R-squared (R^2), Root Mean Squared Error (RMSE) and Mean Absolute Error (MAE) are important metrics for evaluating the performance of regression tasks, their calculation formulas as follows:

$$R^2 = 1 - \frac{\sum_{i=1}^{n}(y_i - \hat{y}_i)^2}{\sum_{i=1}^{n}(\bar{y}_i - y_i)^2} \tag{27}$$

$$RMSE = \sqrt{\frac{1}{n}\sum_{i=1}^{n}(y_i - \hat{y}_i)^2} \quad (28)$$

$$MAE = \frac{1}{n}\sum_{i=1}^{n}|(y_i - \hat{y}_i)| \quad (29)$$

where y_i is the targets, $\hat{y}_i$ is the predicted value, $\bar{y}_i$ is the mean of y_i, n is the number of sample data. R^2, also known as the coefficient of determination, is the ratio of the covariance between predicted and actual values to the variance of the actual values. It measures the proportion of the target variable variance that the model can explain, with values ranging from -1 to 1; closer to 1 indicates better model fit. RMSE is the square root of the mean of the squared differences between targets and predicted values. It gives higher weight to large errors, thus being more sensitive to outliers. MAE represents the average of the absolute differences between targets and predicted values. It reflects the model's prediction error across the entire dataset and is less sensitive to outliers. These metrics play different roles in evaluating regression models, and their comprehensive application aids in a thorough assessment of model performance.

Hyperparameter optimization

In this section, we detail several key hyperparameters of our model. Since the method of dataset partitioning can influence model performance, we randomly divide the dataset into training, validation, and test sets using ratios of 6:2:2 and 8:1:1. Each partitioning strategy is repeated for 10 independent runs with different random seeds to assess model stability and generalizability, of which results can be seen in **Table S3**. Given the limited size of the dataset, an 8:1:1 split is ultimately adopted to balance sufficient training with reliable evaluation. Unlike the 6:2:2 split, which reserves 40% of the data for non-training purposes, the 8:1:1 strategy allocates a larger portion of the valuable labeled data (80%) to model optimization, while still maintaining validation and test sets of adequate size to meet statistical significance requirements. This approach maximizes the utility of the available data and helps prevent potential underfitting caused by an insufficient number of training samples. For all models presented in this work, training is conducted over 200 epochs using the AdamW optimizer [35]. As shown in **Fig.4.(b)**, 200 epochs are sufficient for the convergence of our model.

Learning rate. Learning rate is one of the most important hyperparameters. The initial learning rate is set as $1e^{-3}$, where large learning rate serves the function of implicit regularization, thereby guiding the model to converge towards flat minima associated with better generalization capability. Then, we adopted the step decay strategy (StepLR) [36] for dynamic learning rate adjustment, where the current learning rate is multiplied by a decay factor of 0.1 every 60 training epochs, ensuring fine-grained optimization and stable convergence in the later stages.

The number of convolution layers. The number of layers functions as a double-edged sword: on the one hand, increasing the layer count expands the receptive field, enabling nodes to capture long-range structural dependencies and sophisticated global features; on the other hand, it inherently elevates the risk of over-smoothing. Since GNN layers essentially implement a feature aggregation mechanism analogous to low-pass filtering, stacking an excessive number of layers can drive the hidden representations of all nodes to converge toward identical values. This homogenization erodes the distinctiveness of node-specific features and consequently results in a substantial degradation of model performance. Hence, due to the issue of over-smoothing [37], our model is limited to architectures with 3 to 6 layers. As shown in **Fig.S3(b)**, the impact of the number of GNN layers on the prediction accuracy of E_a. As the number of layers increases from 3 to 5, both RMSE and MAE exhibit a consistent downward trend, reaching their minimum values at 5 layers. This improvement suggests that a moderate increase in network depth enhances the model's capability to capture long-range structural dependencies. However, a significant rebound in prediction errors is observed when the depth further extends to 6 layers. This performance degradation is a classic manifestation of the over-smoothing effect, where excessive aggregation causes node representations to become indistinguishable. Consequently, 5 layers are identified as the optimal architecture for balancing receptive field expansion and feature distinctiveness.

Batch size. This not only determines the speed of model training but also profoundly influences the convergence stability, generalization ability, and memory consumption of the model. We investigate the impact of batch size on model generalization. As illustrated in **Fig.S3(c)**, we evaluate the impact of batch size on the predictive performance of our model. The experimental results indicate that both error metrics follow a U-shaped trend as the batch size increases. The model achieves its peak performance at a batch size of 64, suggesting an optimal trade-off between gradient stability and stochastic exploration. A further increase in batch size leads to a slight

degradation in accuracy, potentially due to the optimization process converging to less generalizable regions of the loss landscape.

Cutoff distances and *Max number of neighbors*. The selection of cutoff distance and maximum number of neighbors represents a trade-off between physical fidelity and model expressivity. An excessively small cutoff may lead to the omission of critical long-range interactions (e.g., van der Waals forces), resulting in loss of information. Conversely, an overly large cutoff or neighbor count may lead to the over-smoothing issue, where node features become indistinguishable as the graph becomes too dense. By optimizing these parameters, we ensure that the graph captures the intrinsic local coordination environment, such as the first and second coordination shells, while avoiding the inclusion of physically insignificant distant nodes, thus enhancing the sensitivity of the model to subtle geometric variations. To investigate the impact of graph construction parameters on model performance, we conduct a sensitivity analysis on the cutoff distance (C) and the maximum number of neighbors (N). As illustrated in **Fig.S3**(d), the model achieves its highest predictive precision at C=8 Å and N=12, where both RMSE and MAE reach their minimum values. Specifically, increasing the cutoff distance from 5 Å to 8 Å (while maintaining N=12) results in a noticeable reduction in error, suggesting that a 5 Å radius is insufficient to capture the long-range interactions and higher-order coordination shells that influence the activation energy. However, at a fixed cutoff of 8 Å, expanding the neighbor limit from N=12 to N=16 leads to a significant degradation in accuracy. This phenomenon can be attributed to the inclusion of physically less relevant distant atoms, which introduces structural noise and causes feature dilution, thereby hindering the model's ability to discern critical local motifs. Consequently, the configuration of C=8 Å and N=12 is identified as the optimal trade-off, providing a comprehensive representation of the chemical environment while maintaining a high signal-to-noise ratio for robust feature extraction.

More details of prediction performance of $SDCGNN_{dk}$ can be seen in **Table S3** to **S6**.

DATA AVAILABILITY

The data that support the findings of this study are not openly available due to reasons of sensitivity and are available from the corresponding author upon reasonable request.

CODE AVAILABILITY

The code and training configurations for SDCGNN and comparative models, as well as the result plotting scripts, are available on GitHub at https://github.com/ZHW-YANN/SDCGNN-DK

ACKNOWLEDGEMENTS

Y.L. acknowledges the support by National Natural Science Foundation of China (92270124) and S.S. acknowledges the support by the National Natural Science Foundation of China (92472207). We acknowledge the High Performance Computing Center of Shanghai University and Shanghai Engineering Research Center of Intelligent Computing System for providing computing resources and technical support.

REFERENCES

1. Li, J., Zhou, M., Wu, H.-H., Wang, L., Zhang, J., Wu, N., Pan, K., Liu, G., Zhang, Y., Han, J., Liu, X., Chen, X., Wan, J. & Zhang, Q. Machine Learning-Assisted Property Prediction of Solid-State Electrolyte. *Adv Energy Mater* **14**, 2304480 (2024).

2. Liu, Y., Guo, B.R., Zou, X.X., Li, Y.J. & Shi, S.Q. Machine learning assisted materials design and discovery for rechargeable batteries. *Energy Storage Mater* **31**, 434–450 (2020).

3. Liu, Y., Zhao, T.L., Ju, W.W. & Shi, S.Q. Materials discovery and design using machine learning. *J Materiomics* **3**, 159–177 (2017).

4. Adhyatma, A., Xu, Y., Hawari, N.H., Satria Palar, P. & Sumboja, A. Improving ionic conductivity of doped $Li_7La_3Zr_2O_{12}$ using optimized machine learning with simplistic descriptors. *Mater Lett* **308**, 131159 (2022).

5. Xu, Y., Zong, Y. & Hippalgaonkar, K. Machine learning-assisted cross-domain prediction of ionic conductivity in sodium and lithium-based superionic conductors using facile descriptors. *J Phys Commun* **4**, 055015 (2020).

6. Katcho, N.A., Carrete, J., Reynaud, M., Rousse, G., Casas-Cabanas, M., Mingo, N., Rodriguez-Carvajal, J. & Carrasco, J. An investigation of the structural properties of Li and Na fast ion conductors using high-throughput bond-valence calculations and machine learning. *J Appl Crystallogr* **52**, 148–157 (2019).

7. Reiser, P., Neubert, M., Eberhard, A., Torresi, L., Zhou, C., Shao, C., Metni, H., van Hoesel, C., Schopmans, H., Sommer, T. & Friederich, P. Graph neural networks for materials science and chemistry. *Commun Mater* **3**, 93 (2022).

8. Cheng, G., Gong, X.-G. & Yin, W.-J. Crystal structure prediction by combining graph network and optimization algorithm. *Nat Commun* **13**, 1492 (2022).

9. Ahmad, Z., Xie, T., Maheshwari, C., Grossman, J.C. & Viswanathan, V. Machine Learning Enabled Computational Screening of Inorganic Solid Electrolytes for Suppression of Dendrite Formation in Lithium Metal Anodes. *ACS Cent Sci* **4**, 996–1006 (2018).

10. Louis, S.-Y., Siriwardane, E.M.D., Joshi, R.P., Omee, S.S., Kumar, N. & Hu, J. Accurate Prediction of Voltage of Battery Electrode Materials Using Attention-Based Graph Neural Networks. *ACS Appl Mater Inter* **14**, 26587–26594 (2022).

11. He, B., Mi, P., Ye, A., Chi, S., Jiao, Y., Zhang, L., Pu, B., Zou, Z., Zhang, W., Avdeev, M., Adams, S., Zhao, J. & Shi, S. A highly efficient and informative method to identify ion transport networks in fast ion conductors. *Acta Mater* **203**, 116490 (2021).

12. Liu, Y., Zou, X., Yang, Z. & Shi, S. Machine learning embedded with materials domain knowledge. *J Chin Ceram Soc* **50**, 863–876 (2022).

13. Liu, Y., Yang, Z., Zou, X., Ma, S., Liu, D., Avdeev, M. & Shi, S. Data quantity governance for machine learning in materials science. *Natl Sci Rev* **10**, nwad125 (2023).

14. Ward, L., Agrawal, A., Choudhary, A. & Wolverton, C. A general-purpose machine learning framework for predicting properties of inorganic materials. *npj Comput Mater* **2**, 16028 (2016).

15. Chen, Z., Liu, Y. & Sun, H. Physics-informed learning of governing equations from scarce data. *Nat Commun* **12**, 6136 (2021).

16. Xie, T. & Grossman, J.C. Crystal graph convolutional neural networks for an accurate and interpretable prediction of material properties. *Phys Rev Lett* **120**, 145301 (2018).

17. Chen, C., Ye, W., Zuo, Y., Zheng, C. & Ong, S.P. Graph Networks as a Universal Machine Learning Framework for Molecules and Crystals. *Chem Mater* **31**, 3564–3572 (2019).

18. Cheng, J., Zhang, C. & Dong, L. A geometric-information-enhanced crystal graph network for predicting properties of materials. *Commun Mater* **2**, 92 (2021).

19. Louis, S.Y., Zhao, Y., Nasiri, A., Wang, X., Song, Y., Liu, F. & Hu, J. Graph convolutional neural networks with global attention for improved materials property prediction. *Phys Chem Chem Phys* **22**, 18141–18148 (2020).

20. Dong, Z., Feng, J., Ji, Y. & Li, Y. SLI-GNN: A Self-Learning-Input Graph Neural Network for Predicting Crystal and Molecular Properties. *Phys Chem A* **127**, 5921–5929 (2023).

21. Meng, K., Huang, C., Wang, Y., Zhang, Y., Li, S., Fang, Z., Wang, H., Wei, S. & Sun, S. BNM-CDGNN: Batch Normalization Multilayer Perceptron Crystal Distance Graph Neural Network for Excellent-Performance Crystal Property Prediction. *J Chem Inf Model* **63**, 6043–6052 (2023).

22. He, B., Ye, A., Chi, S., Mi, P., Ran, Y., Zhang, L., Zou, X., Pu, B., Zhao, Q., Zou, Z., Wang, D., Zhang, W., Zhao, J., Avdeev, M. & Shi, S. CAVD, towards better characterization of void space for ionic transport analysis. *Sci Data* **7**, 153 (2020).

23. Gilmer, J., Schoenholz, S.S., Riley, P.F., Vinyals, O. & Dahl, G.E. Neural message passing for Quantum chemistry. In: International Conference on Machine Learning (2017).

24. Arsalane, S., Kacimi, M., Ziyad, M., Coudurier, G. & Védrine, J.C. Behaviour of copper-thorium phosphate $CuTh_2(PO_4)_3$ in butan-2-ol conversion. *Appl Catal A-Gen* **114**, 243–256 (1994).

25. Cui, W.-J., Yi, J., Chen, L., Wang, C.-X. & Xia, Y.-Y. Synthesis and electrochemical characteristics of NASICON-structured $LiSn_2(PO_4)_3$ anode material for lithium-ion batteries. *J Power Sources* **217**, 77–84 (2012).

26. Wang, L., Sun, X., Ma, J., Chen, B., Li, C., Li, J., Chang, L., Yu, X., Chan, T.-S., Hu, Z.,

Noked, M. & Cui, G. Bidirectionally Compatible Buffering Layer Enables Highly Stable and Conductive Interface for 4.5 V Sulfide-Based All-Solid-State Lithium Batteries. *Adv Energy Mater* **11**, 2100881 (2021).

27. Yang, Z., Liu, Z.,, Zhang, W., Zuo, W., Yu, Z., Zou, X., Yuan, H., Su, Y., Shi, S., Liu, Y. Divide-and-Conquer Machine Learning Embedded with Materials Domain Knowledge. *J Chin Ceram Soc* **54**(2026).

28. He, B., Lai, Z., Wang, D., Liu, X., Liu, Y., Xu, M., Pu, B., Wang, Q., Wang, R., Avdeev, M. & Shi, S. MCTSGT: A graph theory-based Monte Carlo tree strategy for configuration search in disordered structures. *Acta Mater* **302**, 121628 (2026).

29. Schütt, K.T., Arbabzadah, F., Chmiela, S., Müller, K.R. & Tkatchenko, A. Quantum-chemical insights from deep tensor neural networks. *Nat Commun* **8**, 13890 (2017).

30. Kearnes, S., McCloskey, K., Berndl, M., Pande, V. & Riley, P. Molecular graph convolutions: moving beyond fingerprints. *J Comput-Aided Mol Des* **30**, 595–608 (2016).

31. Unke, O.T. & Meuwly, M. PhysNet: A Neural Network for Predicting Energies, Forces, Dipole Moments, and Partial Charges. *J Chem Theory Comput* **15**, 3678–3693 (2019).

32. Kheddar, H., Hemis, M. & Himeur, Y. Automatic speech recognition using advanced deep learning approaches: A survey. *Inform Fusion* **109**, 102422 (2024).

33. Usama, M., Ahmad, B., Song, E., Hossain, M.S., Alrashoud, M. & Muhammad, G. Attention-based sentiment analysis using convolutional and recurrent neural network. *Future Gener Comp Sy* **113**, 571–578 (2020).

34. Mohamed, A., Lee, H.-y., Borgholt, L., Havtorn, J.D., Edin, J., Igel, C., Kirchhoff, K., Li, S.-W., Livescu, K. & Maaløe, L. Self-supervised speech representation learning: A review. *IEEE J Sel Top Signal Process* **16**, 1179–1210 (2022).

35. Loshchilov, I. & Hutter, F. Decoupled Weight Decay Regularization. https://doi.org/10.48550/arXiv.1711.05101 (2017).

36. Paszke, A., Gross, S., Massa, F., Lerer, A., Bradbury, J., Chanan, G., Killeen, T., Lin, Z., Gimelshein, N., Antiga, L., Desmaison, A., Köpf, A., Yang, E.Z., DeVito, Z., Raison, M., Tejani, A., Chilamkurthy, S., Steiner, B., Fang, L., Bai, J. & Chintala, S. PyTorch: An Imperative Style, High-Performance Deep Learning Library. In: Advances in Neural Information Processing Systems (2019).

37. Li, J., Zhang, Q., Liu, W., Chan, A.B. & Fu, Y.G. Another Perspective of Over-Smoothing: Alleviating Semantic Over-Smoothing in Deep GNNs. *IEEE Trans Neural Networks Learn Syst* **36**, 6897–6910 (2025).

AUTHOR CONTRIBUTIONS

Y.L. and Z.Y. conceived and designed the project. Z.Y. and L.W developed and implemented the algorithms under the guidance of Y.L. and S.S.. Z.Y, L.W. and M.A. collected the datasets. Z.Y. and L.W. conducted the experiments, data analysis and method comparisons. Z.Y., L.W. drew the

figures and wrote the manuscript, with the guidance of Y.L. and S.S.. M.A., Y.L. and S.S. finalized the manuscript and figures. S.S. and B.H. gave supports for domain knowledge of materials science and computer science. S.S, Y.L. and M.A. gave suggestions on improving the manuscript. All of the authors reviewed and approved the manuscript.

COMPETING INTERESTS

The authors declare no competing financial or non-financial interests.